

ARTICLE

OPEN



Evidence for topological semimetallicity in a chain-compound TaSe_3

Ahmad Ikhwan Us Saleheen¹, Ramakanta Chapai¹, Lingyi Xing¹, Roshan Nepal¹, Dongliang Gong¹, Xin Gui², Weiwei Xie², David P. Young¹, E. W. Plummer¹ and Rongying Jin¹

Among one-dimensional transition-metal trichalcogenides, TaSe_3 is unconventional in many respects. One is its strong topological semimetallicity as predicted by first-principles calculations. We report the experimental investigations of the electronic properties of one-dimensional-like TaSe_3 single crystals. While the b -axis electrical resistivity shows good metallicity with a high residual resistivity ratio greater than 100, an extremely large magnetoresistance is observed reaching $\approx 7 \times 10^3\%$ at 1.9 K for 14 T. Interestingly, the magnetoresistance follows the Kohler's rule with nearly quadratic magnetic field dependence, consistent with the electron-hole compensation scenario as confirmed by our Hall conductivity data. Both the longitudinal and Hall conductivities show Shubnikov-de Haas oscillations with two frequencies: $F_\alpha \approx 97$ T and $F_\beta \approx 186$ T. Quantitative analysis indicates that F_α results from the two-dimensional-like electron band with the non-trivial Berry phase $[1.1\pi]$, and F_β from the hole band with the trivial Berry phase $[0(3D) - 0.16\pi(2D)]$. Our experimental findings are consistent with the predictions based on first-principles calculations.

npj Quantum Materials (2020)5:53; <https://doi.org/10.1038/s41535-020-00257-7>

INTRODUCTION

Topological materials have ushered in a new era in condensed matter research since the discovery of the quantum Hall effect. Over the years, a few material systems have been reported as topological insulators such as $\text{Bi}_{1-x}\text{Sb}_x$ ¹ and Bi_2Se_3 ², topological semimetals such as Cd_3As_2 ³⁻⁵, Na_3Bi ^{6,7}, YbMnBi_2 ⁸, BaMnSb_2 ⁹, and topological superconductors such as $\text{Cu}_x\text{Bi}_2\text{Se}_3$, $\text{Sn}_{1-x}\text{InTe}$, and others¹⁰⁻¹². In an ordinary semimetal, there is a small overlap between the valence and conduction bands. However, in a topological Dirac semimetal (TDSM), the inverted bands contact only at discrete Dirac points in momentum space with linear energy dispersions. The behavior of these fermions is governed by the relativistic Dirac equation^{13,14}. In a TDSM, spin-orbit coupling (SOC) does not open up a gap, and the Dirac points are protected by the time-reversal and inversion symmetries^{3,15}. If symmetries are broken, these materials can be driven into various other topological phases. For instance, the breaking of either the time-reversal or inversion symmetry can drive a TDSM to a Weyl semimetal³. Moreover, topological materials can also exhibit superconductivity which is an extremely attractive feature for quantum technological applications¹².

One key indication of the possible topological phases in a material is the inversion of energy bands at high-symmetry points in the Brillouin zone¹⁶. These features can be investigated through band structure calculations, which have been quite successful in predicting topological phases in a number of material systems¹⁷⁻²¹. Recently, Nie et al.²² have investigated the topological phases in a chain-compound TaSe_3 through first-principles calculations. The Z_2 invariants (v_0, v_1, v_2, v_3) were obtained for this material, which can be used to distinguish if the system is ordinary or topologically non-trivial. Here, v_0 is called the strong topological index, and a value of $v_0 = 1$ indicates a "strong" topological insulator (STI) phase with an odd number of Dirac cones on the surface, which are robust against weak time-reversal invariant perturbations. A "weak" topological insulator phase is identified when $v_0 = 0$, and

one of the indices v_1, v_2 , or v_3 , known as the weak topological indices, is nonzero¹⁶. The calculations for TaSe_3 revealed the Z_2 invariants (v_0, v_1, v_2, v_3) to be $(1; 100)$ ²², indicating a strong three-dimensional TI with guaranteed Dirac states on the surfaces. Furthermore, band calculations indicate that there is a band inversion even without spin-orbit coupling (SOC) in TaSe_3 ²².

While there have been investigations on various physical properties²³⁻²⁹, the topological properties of TaSe_3 have remained experimentally unexplored, except for a recent preprint³⁰. This is in part due to the multiple bands with two identical electron bands related to band inversion, and one hole band involving no band inversion. In order to distinguish them, information from individual bands has to be separated. In this article, we report the experimental investigation of the Fermi surface topology of TaSe_3 single crystals. Shubnikov-de Haas (SdH) oscillations of both the longitudinal and Hall conductivities are clearly observed. Fast Fourier transformation (FFT) analysis of the SdH oscillations indicates two frequencies, $F_\alpha \approx 97$ T and $F_\beta \approx 186$ T. By constructing the Landau level fan diagram for each oscillation, we obtain the Berry phase $\Phi_\alpha^\alpha \approx 1.1\pi$ and $\Phi_\beta^\beta \approx 0(3D) - 0.16\pi(2D)$. This indicates that the α band is topologically non-trivial, while the β band is trivial. In addition, we observe extremely large magnetoresistance (XMR) in this material which reaches about $7 \times 10^3\%$ for $H = 14$ T at $T = 1.9$ K, and follows the Kohler's scaling law. The quadratic nature of the MR with respect to magnetic field points towards a high degree of electron-hole compensation, supported by our Hall effect data.

RESULTS AND DISCUSSION

Crystal structure and magnetotransport

Figure 1a shows the X-ray diffraction (XRD) pattern for a single crystal of TaSe_3 at room temperature. The XRD peaks are consistent with a monoclinic structure with the space group $P2_1/m$. Due to its malleable nature, the single crystal was not

¹Department of Physics and Astronomy, Louisiana State University, Baton Rouge, LA 70803, USA. ²Department of Chemistry, Louisiana State University, Baton Rouge, LA 70803, USA. email: rjin@lsu.edu

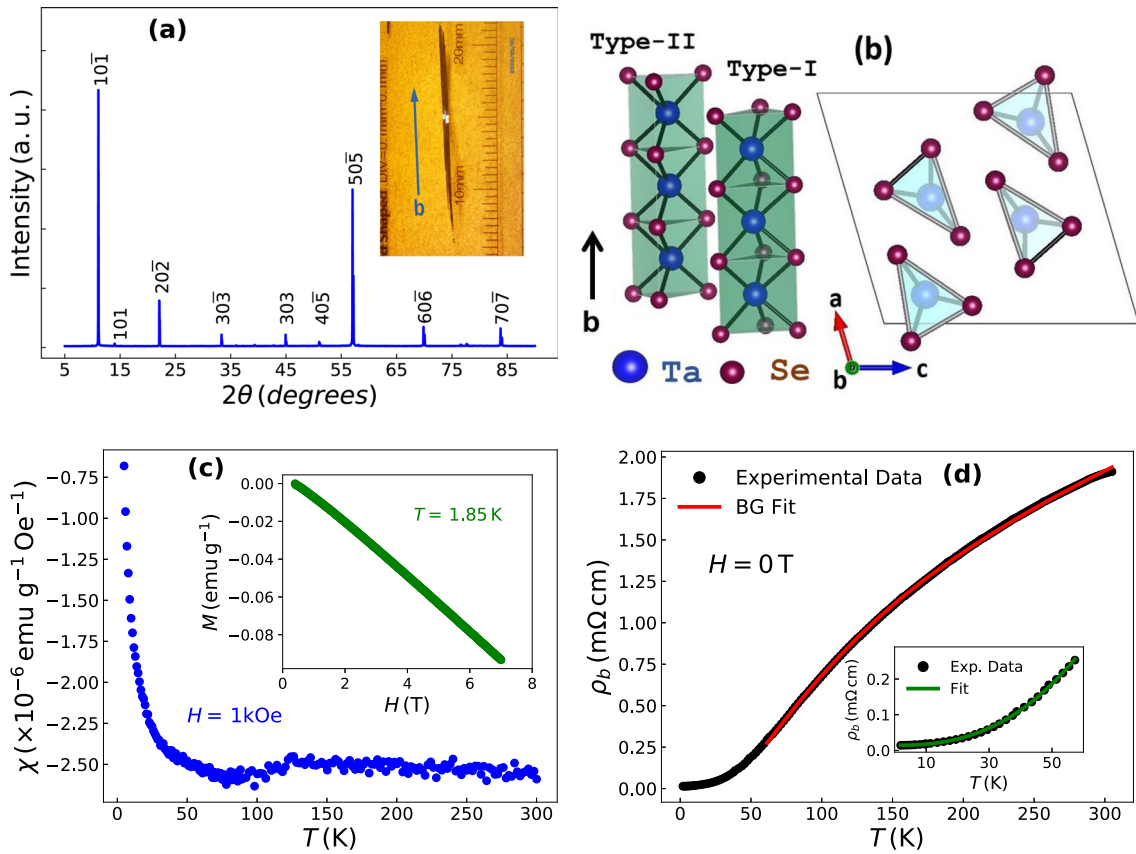


Fig. 1 Crystal structure, magnetization, and electrical resistivity of TaSe₃. **a** XRD pattern of a TaSe₃ single crystal. Inset: Picture of a TaSe₃ single crystal. **b** Crystal structure of TaSe₃. The larger blue and smaller red spheres represent Ta and Se atoms, respectively. **c** Temperature dependence of the magnetic susceptibility [$\chi(T)$] at $H = 1$ kOe. Inset: Magnetic field dependence of the magnetization [$M(H)$] at $T = 1.85$ K. **d** ρ_b vs. temperature (T). Solid red curve indicates the fitting of the data to the Bloch–Grüneisen formula. Inset: $\rho_b(T)$ for $T < 60$ K. The green solid line represents a fit to the formula $\rho_b(T) = \rho_0 + CT^m$ (see text).

perfectly flat on the sample platform, producing a weak $40\bar{5}$ peak at $2\theta \approx 50^\circ$, unexpected from the $10\bar{1}$ plane (Fig. 1a). For further confirmation, we performed single crystal XRD measurements at room temperature, which also revealed the same monoclinic structure. The lattice parameters, $a = 9.834(2)$ Å, $b = 3.496(1)$ Å, $c = 10.421(3)$ Å, and $\beta = 106.237(6)^\circ$ were obtained through a Rietveld refinement of the single crystal XRD data. The crystal structure of TaSe₃ consists of infinite, trigonal prismatic chains along the crystallographic b -axis, as shown in the left side of Fig. 1b. A single linear chain is formed by stacking prismatic cages along the b -axis. At the center of each cage there is a Ta atom, coordinated with six Se atoms at the corners. However, the neighboring chains are inequivalent, which are named as type-I and type-II chains (Fig. 1b). The shorter distance between the Se atoms in type-I chains enables the formation of strong covalent $p-p$ bonding between the two Se atoms, whereas this bond is broken in the type-II chains due to the longer distance. According to band structure calculations, these Se atoms in the type-II chains form bonds with the Ta atoms from the neighboring chains, which is primarily responsible for the band inversion in this material²².

Figure 1c shows the temperature dependence of the magnetic susceptibility [$\chi(T)$] measured at $H = 1$ kOe, which is negative over the entire temperature range. This indicates a diamagnetic behavior in TaSe₃, which is also supported by the negative and linear magnetic field dependence of the magnetization [$M(H)$], measured at $T = 1.85$ K as shown in the inset of Fig. 1c. Since the negative χ is not suppressed up to 7 T, the diamagnetism is not related to superconductivity but to the core electron contribution of TaSe₃.

Figure 1d shows the temperature dependence of the b -axis resistivity (ρ_b) of TaSe₃ at zero magnetic field in the temperature range of 1.9–305 K. The resistivity shows metallic behavior, which decreases with decreasing temperature from ρ_b (300 K) = $1910 \mu\Omega \text{ cm}$ to ρ_b (1.9 K) = $14 \mu\Omega \text{ cm}$. This corresponds to a residual resistivity ratio [RRR = ρ (300 K)/ ρ (1.9 K)] of 136. The RRR of this sample is similar to or exceeds the previously reported values for this material^{23–29}, indicating the high quality of our single crystals. In the temperature range of $T = 60$ –300 K, the $\rho(T)$ data follow the Bloch–Grüneisen (BG) law

$$\rho(T) = \rho_0 + A \left(\frac{T}{\theta_D} \right)^k \int_0^{\theta_D/T} \frac{x^k dx}{(e^x - 1)(1 - e^{-x})}. \quad (1)$$

Here, ρ_0 , A , and θ_D are the residual resistivity, electron–phonon interaction constant, and Debye temperature, respectively. The red solid line in Fig. 1d represents the fitting of the data with Eq. (1). The fitting yields $A = 8.23 \pm 0.03 \text{ m}\Omega \text{ cm}$, $\theta_D = 310 \pm 2$ K, and the exponent $k = 4.6$. The value of k is close to 5 expected for simple metals with dominant electron–phonon scattering. On the other hand, $\rho_b(T)$ at low temperatures ($T < 60$ K) follows a power law behavior given by $\rho_b(T) = \rho_0 + CT^m$, as shown in the inset of Fig. 1d. The residual resistivity $\rho_0 = 14.5 \pm 0.5 \mu\Omega \text{ cm}$ and the exponent $m = 2.5 \pm 0.02$ were obtained from the fit. While there is electron–phonon scattering, it had been argued that in quasi 1D materials, the electron–electron Umklapp scattering can become the dominant scattering mechanism at low temperatures, when the energy ($k_B T$) is smaller than the inter-chain interaction energy^{31,32}. In this scenario, the exponent m takes a value between 2 and 3^{31,32}. Similar behavior was previously reported in

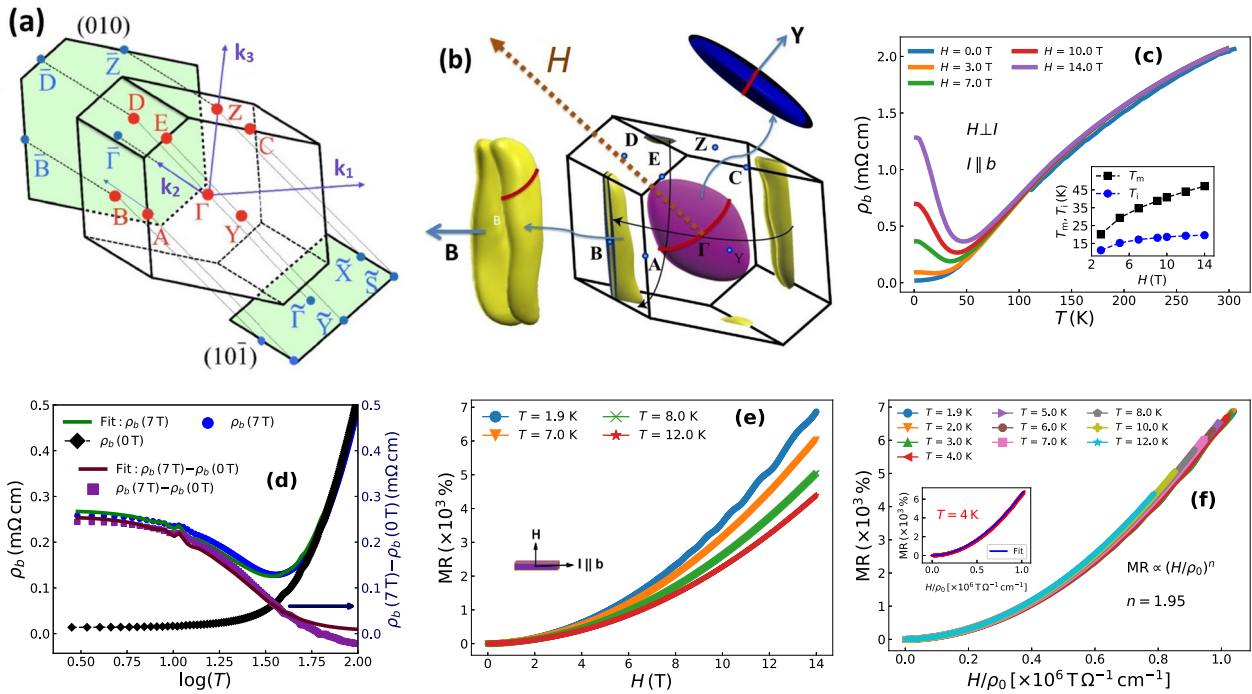


Fig. 2 Brillouin zone, Fermi surface, and magnetotransport measurements. **a** Bulk Brillouin zone (BZ) of TaSe_3 with the high-symmetry points and the projected surface BZ, highlighted in green²². **b** Fermi surface with the hole (purple) and electron (yellow-green) pockets²². The closed electron pockets near the B point and the hole pocket [$-\mathbf{k}_1$ into the page] are enlarged for clarity. The red arrow indicates the applied field direction. The red lines indicate cyclotron orbits for which SdH oscillations were observed. **c** ρ_b vs. T measured at various magnetic fields with $H \perp I$. Inset: H dependence of the two characteristic temperatures: T_m (black squares) is defined as the point where $\partial \rho_b(T, H)/\partial T = 0$ and T_i (blue circles) is where $\partial \rho_b(T, H)/\partial T$ is minimum. **d** Determination of the resistivity change between 0 and 7 T, described by Eq. (3). The black, blue, and purple symbols represent $\rho_b(0\text{ T})$, $\rho_b(7\text{ T})$, and $\rho_b(7\text{ T}) - \rho_b(0\text{ T})$, respectively. The solid green and magenta lines represent fits to Eq. (3) and $\Delta \rho = aH^n/\rho(T, 0)^{n-1}$, respectively. **e** MR vs. H at various temperatures. **f** Kohler's plot of the MR data (MR vs. H/ρ_0) in the temperature range of $T = 1.9\text{--}12\text{ K}$. Inset: MR vs. H/ρ_0 at $T = 4\text{ K}$. The solid blue line represents a fit to Eq. (2). (**a**, **b** are adapted with permission from ref. ²², copyright (2018) by The American Physical Society).

TaSe_3 ³¹. Thus, we consider that the electron-electron Umklapp scattering plays the dominant role in scattering at low temperatures in TaSe_3 .

According to Fig. 1a, the flat surface of the as-grown TaSe_3 single crystals is normal to the $[10\bar{1}]$ direction. For probing the magnetic field (H) effect, we apply H normal to the flat surface, i.e., $H \perp [10\bar{1}]$. For easy discussion, the applied field direction is indicated with respect to the Brillouin zone (BZ) and Fermi surface pockets, as shown in Fig. 2a, b (adapted from ref. ²²), respectively. Figure 2c shows the temperature dependence of ρ_b at various magnetic fields up to 14 T. This and the rest of the measurements were conducted using a sample with RRR = 107. In the presence of an applied magnetic field normal to the current ($H \perp I$), the $\rho_b(T)$ curves maintain metallic behavior at high temperatures, where the resistivity decreases with decreasing temperature until reaching a minimum at T_m . Below this temperature, the resistivity keeps increasing until a plateau-like region is reached at T_i . The onset temperature T_m is identified as the point where $\partial \rho_b(T, H)/\partial T = 0$, whereas T_i is the point where $\partial \rho_b(T, H)/\partial T$ is minimum. The inset of Fig. 2c shows the magnetic field dependence of these two characteristic temperatures, both increasing with increasing magnetic field. However, the increase in the onset temperature T_m is more drastic than that of T_i .

Kohler's scaling law

The magnetic field-induced resistivity upturn and XMR have been frequently observed in topological materials^{33–37}. Several mechanisms are proposed to explain these features, such as field-induced metal-to-insulator transition, electron-hole compensation, topological protection, and so on^{36,38,39}. Recently, it was demonstrated

that this type of field-induced resistivity upturn could be explained within the framework of the Kohler's scaling law without invoking any topological considerations^{35,40}. The Kohler's scaling law is given by^{41,42}

$$\text{MR} = a(H/\rho_0)^n \quad (2)$$

with a and n being constants. Since MR is given by $\frac{\rho(T, H) - \rho(T, 0)}{\rho(T, 0)}$, Eq. (2) can be rearranged and written as

$$\rho(T, H) = \rho(T, 0) + a \frac{H^n}{\rho(T, 0)^{n-1}}. \quad (3)$$

In light of Eq. (3), $\rho(T, H)$ consists of two terms: temperature dependence of the resistivity at zero field [$\rho(T, 0)$] and the magnetic-field-induced resistivity [$\Delta \rho = aH^n/\rho(T, 0)^{n-1}$]. Since these two terms have opposite temperature dependence, the minimum in the $\rho(T, H)$ curve arises due to a competition between the two terms^{35,40,43}. For demonstration, we choose $\rho_b(T)$ at $H = 7\text{ T}$, as shown by the blue symbols in Fig. 2d. The solid green line in the figure represents a fit of the data to Eq. (3) with $a = 1.3 \times 10^{-10} (\Omega \text{ cm})^n T^{-n}$ and $n = 1.95$. The purple symbols in Fig. 2d represent the difference in the temperature dependence of the resistivity measured at $H = 0$ and 7 T [$\Delta \rho = \rho_b(7\text{ T}) - \rho_b(0\text{ T})$]. The data was fitted with the second term in Eq. (3), as represented by the solid (magenta) line. We note that Eq. (3) can describe the field-induced resistivity fairly well. Furthermore, the plateau in the $\rho_b(T, H)$ curves (Fig. 2c) at low temperatures can also be explained through Eq. (3). At low temperatures, $\rho_b(T, 0) = \rho_0$ becomes very low and practically temperature independent. Therefore, $\rho(T, H) \sim aH^n/\rho_0^{n-1}$ is constant at low temperatures, giving rise to a plateau.

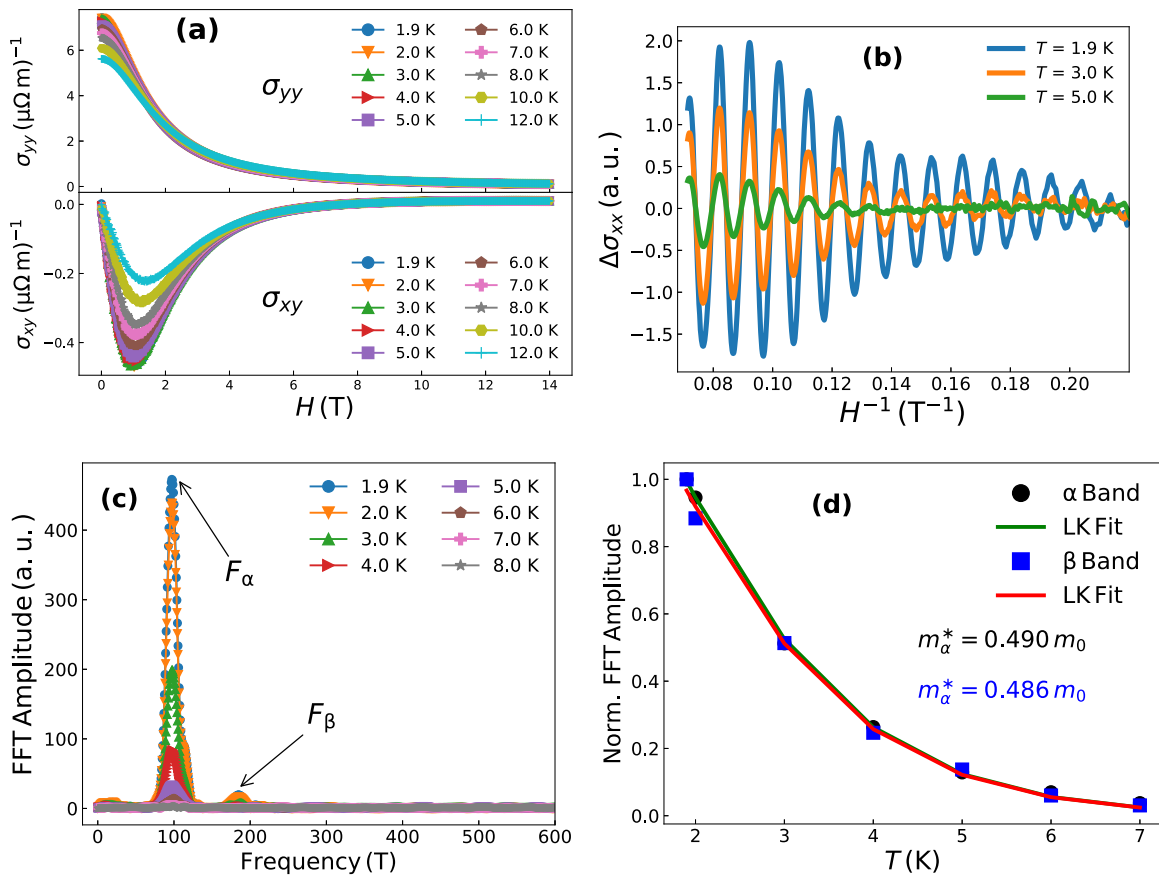


Fig. 3 Conductivity and SdH oscillations. **a** Longitudinal conductivity (σ_{yy}) (upper panel) and Hall conductivity (σ_{xy}) (bottom panel) of TaSe_3 for a field range of $H = 0\text{--}14\text{ T}$ at various temperatures. **b** Oscillatory conductivity ($\Delta\sigma_{yy}$) vs. inverse magnetic field (H^{-1}) at indicated temperatures. **c** FFT spectrum of the oscillations at various temperatures. **d** The temperature dependence of the FFT amplitudes of the two principal frequencies (F_α and F_β) in the FFT spectra. Solid lines represent fits to Eq. (5).

To confirm the Kohler's scaling law, we have measured the magnetic field dependence of $\rho_b(T, H)$ at fixed temperatures with $H \perp I$. Since the measured $\rho_b(T, H)$ can contain both the longitudinal (ρ_{yy}) and Hall (ρ_{xy}) contributions, the longitudinal component was isolated from the Hall component by using the relation, $\rho_{yy} = [\rho_b(T, +H) + \rho_b(T, -H)]/2$. The MR was then calculated using the standard relation, $\text{MR} = [\rho_{yy}(H) - \rho_{yy}(0)]/\rho_{yy}(0)$. Figure 2e shows the MR at indicated temperatures for up to 14 T. We observe the XMR in this material which reaches about $7 \times 10^3\%$ at $T = 1.9\text{ K}$ and $H = 14\text{ T}$ without showing any sign of saturation. This is comparable to other XMR materials, such as Cd_3As_2 ⁴⁴, Na_3Bi ⁴⁵, NbP ⁴⁶, TaAs ⁴⁷, WTe_2 ^{33,38}, and PtBi_{2-x} ³⁷.

The Kohler's scaling law (Eq. (2)) can describe the motion of electrons in magnetic field for a single band or multiple bands with electron-hole compensation^{35,41,42}. For $n = 2$, the Kohler's law [$\text{MR} = a(H/\rho_0)^2$] can be derived from the two-band model of the electrical resistivity for non-magnetic materials, when the electron and hole carrier concentration is perfectly compensated³⁵. However, Wang et al.³⁵ also argued that MR for an imperfectly compensated system can still obey the Kohler's law if either or both the mobilities are small. Nevertheless, this law would be violated if a is temperature dependent³⁵. Figure 2f shows the MR at various temperatures plotted against the rescaled magnetic field H/ρ_0 . Consequently, all the MR curves from $T = 1.9\text{--}12\text{ K}$ collapse on to a single curve, indicating that the scattering mechanism is the same throughout the relevant temperature and field ranges. This rules out the possibility of a metal-to-insulator transition^{35,36,48}. In addition, the collapse of the MR curves, according to the Kohler's rule, indicates that the carrier concentration and the mobility ratio of hole-to-electron do not

change significantly with temperature^{49,50}. The inset of Fig. 2f shows a fitting of the MR curve at $T = 4\text{ K}$ using Eq. (2), yielding $a = (1.30 \pm 0.01) \times 10^{-10} (\Omega \text{ cm})^n T^{-n}$ and $n = 1.950 \pm 0.001$. These values are used to fit the $\rho_b(T)$ data, as shown in Fig. 2d. The value of n depends on the level of carrier compensation. For a system with perfect electron-hole compensation, n should be 2^{35,43}. Thus, the value of $n = 1.95$ for TaSe_3 points towards a high degree of electron-hole compensation.

SdH oscillations

As can be seen in Fig. 2e, ρ_b exhibits SdH oscillations. The SdH oscillations occur in crystalline solids when the density of states is periodically modulated as a function of magnetic field due to the Landau quantization of the energy states in magnetic field⁵¹. One of the most useful aspects of SdH oscillations is that it contains information on band topology reflected in the Berry phase. A widely used method to extract the Berry phase is to construct the Landau level fan diagram, where the minima in the SdH oscillations of the conductivity are assigned to an integer Landau level index⁵¹. We calculated the longitudinal (σ_{yy}) and Hall conductivities (σ_{xy}) using the following relations:

$$\sigma_{yy} = \frac{\rho_{yy}}{\rho_{yy}^2 + \rho_{xy}^2}, \quad (4)$$

$$\sigma_{xy} = -\frac{\rho_{xy}}{\rho_{yy}^2 + \rho_{xy}^2}.$$

Figure 3a shows the longitudinal and Hall conductivities measured at various temperatures for $H = 0\text{--}14\text{ T}$. The smooth background of the $\sigma_{yy}(H)$ data was deduced through polynomial fitting, which was then subtracted from the data to obtain the oscillatory

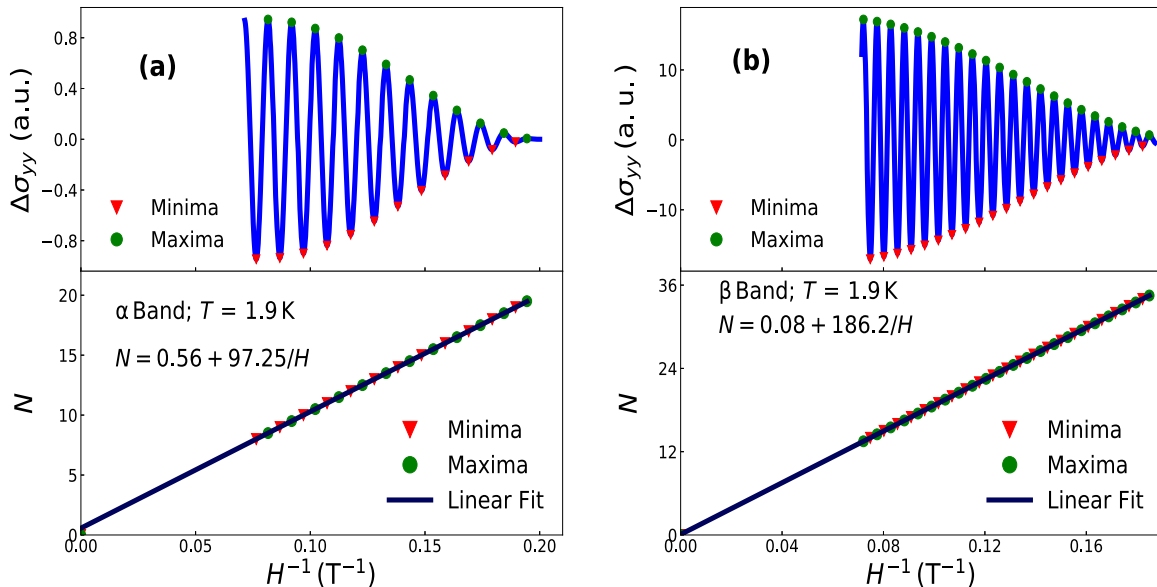


Fig. 4 Landau level fan diagrams. **a** Landau level fan diagram for the α band at $T = 1.9$ K, where N is obtained from $\Delta\sigma_{yy}$ and plotted as a function of H^{-1} . Solid line represents a linear fit to the data. **b** The Landau level fan diagram for the β band at $T = 1.9$ K.

component of the conductivity $\Delta\sigma_{yy}$. Figure 3b shows $\sigma_{yy}(H)$ vs. H^{-1} at indicated temperatures. FFT analysis reveals two frequencies with $F_\alpha \approx 97$ T and $F_\beta \approx 186$ T, as shown in Fig. 3c. The FFT frequency (F) and the Fermi surface cross-section (A_F) are related by the Onsager relation $F = (\hbar/2\pi e)A_F$. Therefore, F_α and F_β correspond to $A_\alpha = 0.009 \text{ \AA}^{-2}$ and $A_\beta = 0.018 \text{ \AA}^{-2}$, respectively. In Fig. 2b, the cyclotron orbits perpendicular to the H direction are depicted by red lines for both electron (yellow-green) and hole (purple) pockets. Note that the two electron pockets are identical²², thus having the same frequency, i.e., F_α . Since the cross-sections are not perfectly circular, it is difficult to accurately estimate the corresponding Fermi wave vectors from the measured cross-section areas.

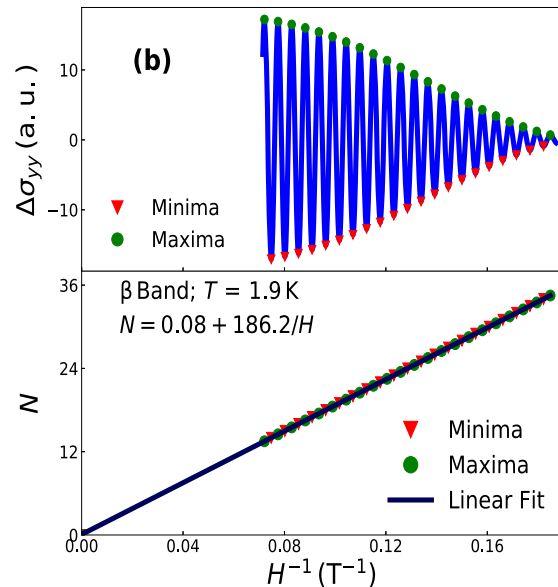
Figure 3d shows the temperature dependence of the normalized FFT amplitudes for the α and β bands. The gradual damping of the oscillation amplitudes with increasing temperature can be described by the Lifshitz-Kosevich (LK) equation^{51–53}

$$R_T = \frac{A'(m^*/m_0)T}{\sinh[A'(m^*/m_0)T]} \quad (5)$$

Here, R_T , m_0 , and m^* are the FFT amplitude, free electron mass, and effective mass, respectively. The parameter A' is given by $A' = \frac{2\pi^2 k_B m_0}{e\hbar H_{\text{eff}}}$, where $H_{\text{eff}} = 2/(1/H_1 + 1/H_2)$, with $H_1 = 5$ T and $H_2 = 14$ T being the lower and upper limits of the magnetic field range in which the FFT analysis was conducted. k_B and \hbar are the Boltzmann and Planck constants, respectively. We obtain the effective masses of $m_\alpha^* = 0.49m_0$ and $m_\beta^* = 0.48m_0$ corresponding to the α and β bands though fitting the FFT amplitude vs. temperature data with Eq. (5), as shown in Fig. 3d.

Berry phase

We have isolated the oscillations corresponding to each frequency (F_α and F_β) through filtering, and the isolated single frequency oscillations were used to construct the Landau level fan diagram as shown in Fig. 4a, b. The minima in $\Delta\sigma_{yy}(H^{-1})$ positions are assigned integer Landau level indices (N), whereas the maxima positions are assigned $N + 1/2$. According to the Lifshitz-Onsager relationship, $N = F/H + \Phi_B/2\pi + \delta$ ^{51,52}. Here, Φ_B is the Berry phase, and δ depends on the dimensionality of the Fermi surface and carrier type. For a two-dimensional (2D) Fermi surface $\delta = 0$, whereas $\delta = +1/8(-1/8)$ for the minima (maxima) of a three-



dimensional (3D) electron band. On the other hand, $\delta = -1/8(+1/8)$ for the minima (maxima) of a 3D hole band. It implies from the Onsager relationship that the slope of $N(H^{-1})$ plot should correspond to the oscillation frequency, while the intercept can be used to calculate Φ_B . The slopes of the straight lines were found to be 97.25 ± 0.03 and 186.2 ± 0.01 T for the α and β bands, respectively. These values are in excellent agreement with the oscillation frequencies identified through FFT analysis. The intercepts were found to 0.56 ± 0.004 and 0.08 ± 0.002 for the α and β bands, respectively. According to band structure calculations²², the α band is 2D (see Fig. 2b). Thus, the corresponding Berry phase is $\Phi_\alpha^B = [0.56 \pm 0.004] \times 2\pi \approx [1.120 \pm 0.008]\pi$. This indicates a non-trivial topology for the α band. On the other hand, the β band is predicted to be hole-like with the 3D characteristic (see Fig. 2b). With $H \perp [10\bar{1}]$, F_β corresponds to the maxima of the β Fermi pocket, with $\delta = +1/8$. Thus, we obtain $\Phi_\beta^B(3D) = [(0.08 \pm 0.002) - 1/8] \times 2\pi = [-0.09 \pm 0.003]\pi \approx 0$. Since it is disc shaped (Fig. 2b), $\Phi_\beta^B(2D) = [0.08 \pm 0.002] \times 2\pi \approx [0.160 \pm 0.004]\pi$ using $\delta = 0$. The non-trivial Berry phase for the α band and a trivial one for the β band are consistent with first-principles calculations²². Interestingly, an oscillation frequency of 175 T was identified to correspond to a non-trivial band in ref. ³⁰. At present, it is unclear whether the slight frequency difference can make such a dramatic change in the topology of the β band.

Hall effect and two-band fitting

To further understand the electronic structure of TaSe₃, we have investigated the Hall effect at low temperatures. Figure 5a shows the results of Hall resistivity (ρ_{xy}) measurements up to $H = 14$ T between temperatures $T = 1.9$ –8 K. The field dependence of the Hall resistivity [$\rho_{xy}(H)$] shows a non-linear behavior, which changes from positive at lower fields to negative at high fields ($H > 7.5$ T). This behavior suggests that both types of charge carriers are responsible for the Hall effect. The $\rho_{xy}(H)$ curves are almost identical in the temperature range of $T = 1.9$ –8 K, indicating that the carrier concentrations and mobilities do not significantly change in this temperature range⁵⁰. Clear SdH oscillations can be seen for $H > 9$ T, especially at low temperatures. Since $\rho_{xy} \ll \rho_{yy}$, multiple band analysis of the Hall data should be conducted through the Hall conductivity σ_{xy} ^{50,51}, which was calculated through Eq. (4). For a system with multi-band transport, σ_{xy} can

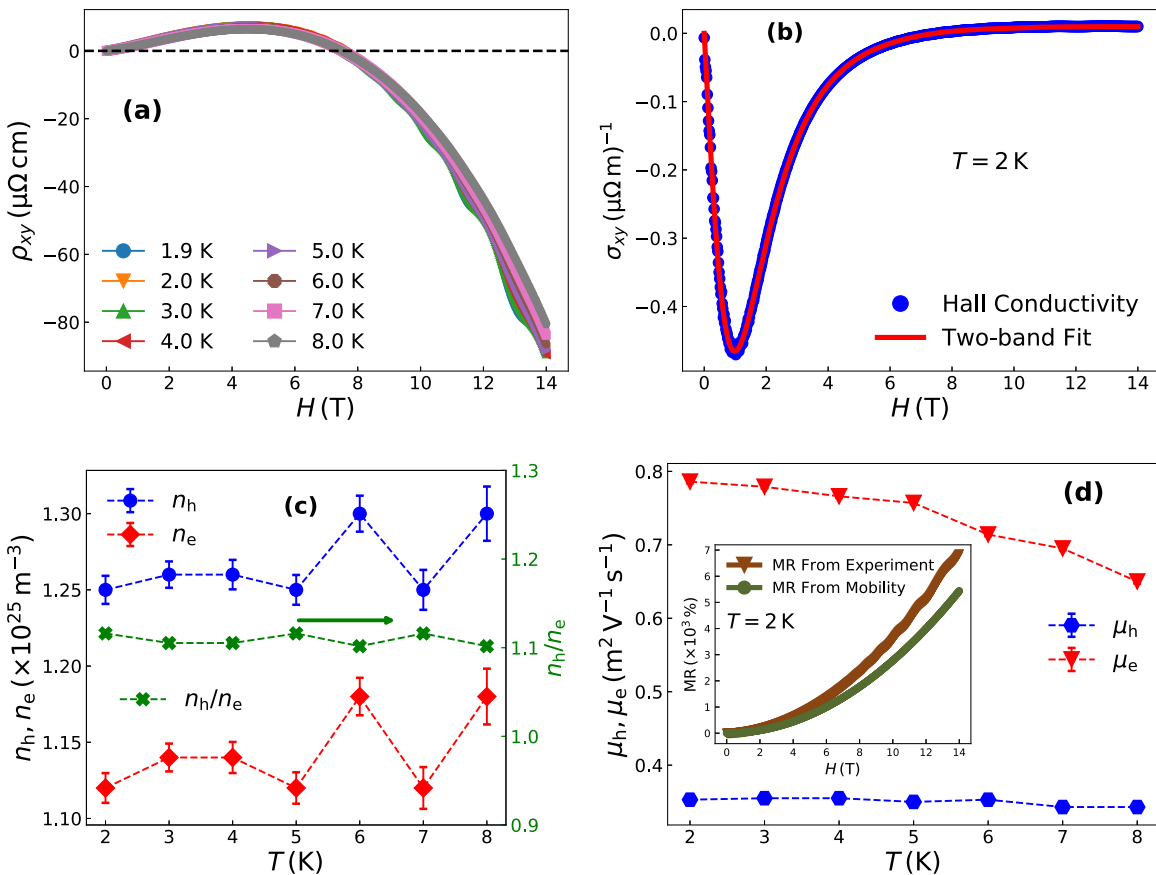


Fig. 5 Hall effect and two-band fitting. **a** Hall resistivity (ρ_{xy}) vs. H at various temperatures. **b** Hall conductivity (σ_{xy}) vs. H at $T = 2$ K. Solid red line represents a fit to the two-band model (Eq. (6)). **c** Temperature dependence of hole and electron concentrations (left vertical axis) and n_h/n_e (right vertical axis). **d** Temperature dependence of the mobilities of the holes and electrons. Inset: MR vs. H at $T = 2$ K from experiment [$MR = \frac{\rho(H) - \rho(0)}{\rho(0)}$] and mobilities [$MR = \mu_h \mu_e H^2$], represented by the brown and green lines, respectively. The error bars in **c**, **d** represent standard errors obtained through fitting the experimental data to Eq. (6).

be expressed as

$$\sigma_{xy} = eH \left[\frac{n_h \mu_h^2}{1 + (\mu_h H)^2} - \frac{n_e \mu_e^2}{1 + (\mu_e H)^2} \right]. \quad (6)$$

Here, $n_h(n_e)$, $\mu_h(\mu_e)$ are the concentration of holes (electrons) and mobilities of holes (electrons), respectively. Figure 5b shows the magnetic field dependence of the Hall conductivity at $T = 2$ K, and the corresponding fitting using Eq. (6). We can see that the two-band model fits the $\sigma_{xy}(H)$ data at $T = 2$ K quite well. Similarly, Eq. (6) generated good fits for the $\sigma_{xy}(H)$ data in the temperature range of $T = 2\text{--}8$ K. The carrier concentrations and mobilities were obtained from fitting, and their temperature dependence in the range of $T = 2\text{--}8$ K is shown in Fig. 5c, d. The hole concentration remains slightly higher than the electron concentration throughout the temperature range, whereas the mobility of the electrons remains higher than that of holes. From the semiclassical two-band model, the MR of non-magnetic materials with perfectly compensated electron and hole-type carriers ($n_h = n_e$) can be described by $MR \approx \mu_e \mu_h H^2$ ^{35,54,55}. We have used the carrier mobilities obtained from the Hall conductivity data to estimate the MR at various temperatures through this relation. The MR curves estimated from the mobilities are remarkably similar to that obtained from experiment, as demonstrated in the inset Fig. 5d for $T = 2$ K. The slight difference between them could be due to the imperfect carrier compensation in TaSe₃.

At $T = 2$ K, the fitting yielded the hole and electron concentrations: $n_h = 1.25 \times 10^{19} \text{ cm}^{-3}$, $n_e = 1.12 \times 10^{19} \text{ cm}^{-3}$, and mobilities

$\mu_h = 3.6 \times 10^3 \text{ cm}^2 \text{ V}^{-1} \text{ s}^{-1}$, $\mu_e = 7.8 \times 10^3 \text{ cm}^2 \text{ V}^{-1} \text{ s}^{-1}$. The relatively low carrier concentrations are consistent with the semimetallic nature of TaSe₃. For TaSe₃, the relatively lower mobility ($\approx 10^3 \text{ cm}^2 \text{ V}^{-1} \text{ s}^{-1}$) is due to its relatively “heavier” effective mass ($m^* \approx 0.49 m_0$) compared to other semimetals ^{4,34,36,50,56,57}. In the temperature range of $T = 2\text{--}8$ K, the ratio $n_h/n_e \approx 1.1$, as shown in Fig. 5c. This feature points towards a high degree of carrier compensation, making the Kohler’s scaling law well justified (Fig. 2f).

To summarize, we have grown single crystals of a chain-compound TaSe₃ through the chemical vapor transport method. We observed the XMR effect in this material which reaches up to $7 \times 10^3\%$ at $T = 1.9$ K for $H = 14$ T applied normal to the *b*-axis. The XMR obeys the Kohler’s scaling law as evident from the collapse of the MR curves measured at different temperatures on to a single curve when plotted as $MR = a(H/\rho_0)^n$. Furthermore, both the longitudinal and Hall conductivities exhibit SdH oscillations at low temperatures. A FFT analysis of the SdH oscillations of the electrical conductivity revealed two fundamental frequencies, $F_\alpha \approx 97$ T and $F_\beta \approx 186$ T. The Berry phases $\Phi_\alpha^\alpha \approx 1.1\pi$ and $\Phi_\beta^\beta \approx 0(3D) - 0.16\pi(2D)$ for the corresponding α and β bands were extracted through the construction of Landau level fan diagrams. This indicates the non-trivial Berry phase for the α band and the trivial one for the β band. Comparing with band structure calculations ²², we found that the non-trivial α band is the 2D electron pocket, whereas the trivial β band represents the hole pocket. An analysis of the Hall conductivity revealed two types of carriers, whose concentrations and mobilities were calculated. The obtained electron and hole concentrations are very close, pointing towards

a nearly perfect electron–hole compensation in this material. The XMR is likely to have originated from this nearly perfect carrier compensation.

Compared to other TDSMs, a distinguishing feature of TaSe_3 is its quasi 1D crystal structure. As predicted in ref. ²², this unique structure can host various topological phases, such as 3D STI, 3D WTI, and Dirac semimetal phases under different strains. It is thus an ideal material system for studying the structure–topological property relationship. Future investigations into the strain or pressure effects on TaSe_3 could offer valuable new insights.

METHODS

Sample synthesis

Single crystals of TaSe_3 were grown through the chemical vapor transport method. High purity (better than 99.9%) powder of Ta and Se with a molar ratio of 1:3.3 were mixed together and pressed into a pellet. The excess Se acts as the transport agent. The pellet was sealed in an evacuated quartz tube, and placed into a horizontal tube furnace. The end of the quartz tube with the pellet (starting material) was placed in the middle of the tube furnace and heated to 700 °C. The other end of the tube furnace was kept open to the atmosphere, which acted as the cold end, and thus creating a temperature gradient necessary for vapor transport. The furnace was maintained at 700 °C for 14 days, followed by a slow cooling to room temperature. Finally, thin 1D-like single crystals with shiny surfaces were obtained.

Measurements

Single crystal XRD measurements were carried out at room temperature using a Bruker Kappa Apex-II and a PANalytical Empyrean X-ray diffractometer. Electrical resistivity and Hall effect measurements were carried out using the standard four-probe technique in a physical property measurement system (PPMS, Quantum Design) for up to 14 T, and in a temperature range of $T = 1.9\text{--}305$ K. The electrical contacts were made using gold wires attached to the sample through epoxy. Hall effect data were measured in both positive and negative field and then subtracted to eliminate the lead-offset voltage.

DATA AVAILABILITY

All data that support the findings of this study are available from the corresponding author upon reasonable request.

Received: 3 April 2020; Accepted: 9 July 2020;

Published online: 24 July 2020

REFERENCES

1. Hsieh, D. et al. A tunable topological insulator in the spin helical Dirac transport regime. *Nature* **460**, 1101–1105 (2009).
2. Xia, Y. et al. Observation of a large-gap topological-insulator class with a single Dirac cone on the surface. *Nat. Phys.* **5**, 398–402 (2009).
3. Liu, Z. K. et al. A stable three-dimensional topological Dirac semimetal Cd_3As_2 . *Nat. Mater.* **13**, 677–681 (2014).
4. Neupane, M. et al. Observation of a three-dimensional topological Dirac semimetal phase in high-mobility Cd_3As_2 . *Nat. Commun.* **5**, 3786 (2014).
5. Zheng, G. et al. Transport evidence for the three-dimensional Dirac semimetal phase in ZrTe_5 . *Phys. Rev. B* **93**, 115414 (2016).
6. Liu, Z. K. et al. Discovery of a three-dimensional topological Dirac semimetal, Na_3Bi . *Science* **343**, 864–867 (2014).
7. Xu, S.-Y. et al. Observation of Fermi arc surface states in a topological metal. *Science* **347**, 294–298 (2015).
8. Liu, J. Y. et al. A magnetic topological semimetal $\text{Sr}_{1-y}\text{Mn}_{1-z}\text{Sb}_2$ ($y, z < 0.1$). *Nat. Mater.* **16**, 905–910 (2017).
9. Huang, S., Kim, J., Shelton, W. A., Plummer, E. W. & Jin, R. Nontrivial Berry phase in magnetic BaMnSb_2 semimetal. *Proc. Natl. Acad. Sci. USA* **114**, 6256–6261 (2017).
10. Hor, Y. S. et al. Superconductivity in $\text{Cu}_x\text{Bi}_2\text{Se}_3$ and its implications for pairing in the undoped topological insulator. *Phys. Rev. Lett.* **104**, 057001 (2010).
11. Sasaki, S. et al. Odd-parity pairing and topological superconductivity in a strongly spin-orbit coupled semiconductor. *Phys. Rev. Lett.* **109**, 217004 (2012).
12. Sato, M. & Ando, Y. Topological superconductors: a review. *Rep. Prog. Phys.* **80**, 076501 (2017).
13. Dirac, P. A. M. *The Principles of Quantum Mechanics* Ch. 11 (Oxford Univ. Press, Oxford, 1958).
14. Hasan, M. Z. & Kane, C. L. Colloquium: topological insulators. *Rev. Mod. Phys.* **82**, 3045–3067 (2010).
15. Borisenko, S. et al. Experimental realization of a three-dimensional Dirac semimetal. *Phys. Rev. Lett.* **113**, 027603 (2014).
16. Bansil, A., Lin, H. & Das, T. Colloquium: topological band theory. *Rev. Mod. Phys.* **88**, 021004 (2016).
17. Fu, L. & Kane, C. L. Topological insulators with inversion symmetry. *Phys. Rev. B* **76**, 045302 (2007).
18. Zhang, H. et al. Topological insulators in Bi_2Se_3 , Bi_2Te_3 and Sb_2Te_3 with a single Dirac cone on the surface. *Nat. Phys.* **5**, 438–442 (2009).
19. Hsieh, T. H. et al. Topological crystalline insulators in the SnTe material class. *Nat. Commun.* **3**, 982 (2012).
20. Wang, Z. et al. Dirac semimetal and topological phase transitions in A_3Bi ($\text{A} = \text{Na}, \text{K}, \text{Rb}$). *Phys. Rev. B* **85**, 195320 (2012).
21. Wang, Z., Weng, H., Wu, Q., Dai, X. & Fang, Z. Three-dimensional Dirac semimetal and quantum transport in Cd_3As_2 . *Phys. Rev. B* **88**, 125427 (2013).
22. Nie, S. et al. Topological phases in the TaSe_3 compound. *Phys. Rev. B* **98**, 125143 (2018).
23. Nomura, A., Yamaya, K., Takayanagi, S., Ichimura, K. & Tanda, S. Effect of Cu doping on superconductivity in TaSe_3 : relationship between superconductivity and induced charge density wave. *EPL* **124**, 67001 (2019).
24. Haen, P., Lapierre, F., Monceau, P., Regueiro, M. N. & Richard, J. Low temperature phase transition in the chain-like compounds NbSe_3 and TaSe_3 . *Solid State Commun.* **26**, 725–730 (1978).
25. Yamamoto, M. Superconducting properties of TaSe_3 . *J. Phys. Soc. Jpn* **45**, 431–438 (1978).
26. Rashid, M. H. & Sellmyer, D. J. Electrical conduction in quasi-one-dimensional compounds: TaSe_3 , Nb_3Se_3 , and Nb_3S_4 . *Phys. Rev. B* **29**, 2359–2362 (1984).
27. Fleming, R. M., Polo, J. A. & Coleman, R. V. Oscillatory magnetotransport in NbSe_3 and TaSe_3 . *Phys. Rev. B* **17**, 1634–1644 (1978).
28. Fisher, B. & Fibich, M. Transport properties of TaSe_3 . *Phys. Rev. B* **37**, 2820–2825 (1988).
29. Fisher, B. Thermoelectric power and elastoresistance of TaSe_3 . *Phys. Rev. B* **35**, 2687–2689 (1987).
30. Xia, W. et al. Bulk Fermi surface of the layered superconductor TaSe_3 with three-dimensional strong topological insulator state. *Phys. Rev. B* **101**, 155117 (2020).
31. Nagata, S., Kutsuzawa, H., Ebisu, S., Yamamura, H. & Taniguchi, S. Superconductivity in the quasi-one-dimensional conductor TaSe_3 . *J. Phys. Chem. Solids* **50**, 703–707 (1989).
32. Oshiyama, A., Nakao, K. & Kamimura, H. Electrical resistivity due to electron-electron scattering in quasi-one-dimensional metals. *J. Phys. Soc. Jpn* **45**, 1136–1146 (1978).
33. Ali, M. N. et al. Large, non-saturating magnetoresistance in WTe_2 . *Nature* **514**, 205–208 (2014).
34. Ali, M. N. et al. Correlation of crystal quality and extreme magnetoresistance of WTe_2 . *EPL* **110**, 67002 (2015).
35. Wang, Y. L. et al. Origin of the turn-on temperature behavior in WTe_2 . *Phys. Rev. B* **92**, 180402 (2015).
36. Sudesh, P. K. & Patnaik, S. Origin of exceptional magneto-resistance in Weyl semimetal TaSb_2 . *J. Phys. Commun.* **3**, 115007 (2019).
37. Xing, L., Chapai, R., Nepal, R. & Jin, R. Topological behavior and Zeeman splitting in trigonal PtBi_{2-x} single crystals. *npj Quantum Mater.* **5**, 10 (2020).
38. Fallah Tafti, F. et al. Temperature-field phase diagram of extreme magnetoresistance. *Proc. Natl. Acad. Sci. USA* **113**, E3475–E3481 (2016).
39. Tafti, F. F., Gibson, Q. D., Kushwaha, S. K., Haldolaarachchige, N. & Cava, R. J. Resistivity plateau and extreme magnetoresistance in LaSb . *Nat. Phys.* **12**, 272–277 (2016).
40. Han, F. et al. Separation of electron and hole dynamics in the semimetal LaSb . *Phys. Rev. B* **96**, 125112 (2017).
41. Kohler, M. Zur magnetischen widerstandsänderung reiner metalle. *Ann. Phys. (Berl.)* **424**, 211–218 (1938).
42. Pippard, A. B. *Magnetoresistance in Metals* Ch. 1 (Cambridge Univ. Press, Cambridge, 1989).
43. Pavlosiuk, O., Swatek, P., Kaczorowski, D. & Wiśniewski, P. Magnetoresistance in LuBi and YBi semimetals due to nearly perfect carrier compensation. *Phys. Rev. B* **97**, 235132 (2018).
44. Narayanan, A. et al. Linear magnetoresistance caused by mobility fluctuations in n -doped Cd_3As_2 . *Phys. Rev. Lett.* **114**, 117201 (2015).

45. Xiong, J. et al. Evidence for the chiral anomaly in the Dirac semimetal Na_3Bi . *Science* **350**, 413–416 (2015).
46. Shekhar, C. et al. Extremely large magnetoresistance and ultrahigh mobility in the topological Weyl semimetal candidate NbP . *Nat. Phys.* **11**, 645–649 (2015).
47. Huang, X. et al. Observation of the chiral-anomaly-induced negative magnetoresistance in 3D Weyl semimetal TaAs . *Phys. Rev. X* **5**, 031023 (2015).
48. Jo, N. H. et al. Extremely large magnetoresistance and Kohler's rule in PdSn_4 : a complete study of thermodynamic, transport, and band-structure properties. *Phys. Rev. B* **96**, 165145 (2017).
49. Sun, S., Wang, Q., Guo, P.-J., Liu, K. & Lei, H. Large magnetoresistance in LaBi : origin of field-induced resistivity upturn and plateau in compensated semimetals. *N. J. Phys.* **18**, 082002 (2016).
50. Pavlosiuk, O., Swatek, P. & Wisniewski, P. Giant magnetoresistance, three-dimensional fermi surface and origin of resistivity plateau in YSb semimetal. *Sci. Rep.* **6**, 38691 (2016).
51. Ando, Y. Topological insulator materials. *J. Phys. Soc. Jpn* **82**, 102001 (2013).
52. Shoenberg, D. *Magnetic Oscillations in Metals*. (Cambridge Univ. Press, Cambridge, 1984).
53. Chapai, R. et al. Fermions and bosons in nonsymmorphic PdSb_2 with sixfold degeneracy. *Phys. Rev. B* **99**, 161110 (2019).
54. Ashcroft, N. W. & Mermin, N. D. *Solid State Physics* (Saunders College Publishing, Philadelphia, 1976).
55. Guo, P.-J., Yang, H.-C., Zhang, B.-J., Liu, K. & Lu, Z.-Y. Charge compensation in extremely large magnetoresistance materials LaSb and LaBi revealed by first-principles calculations. *Phys. Rev. B* **93**, 235142 (2016).
56. Pavlosiuk, O. & Kaczorowski, D. Galvanomagnetic properties of the putative type-II Dirac semimetal PtTe_2 . *Sci. Rep.* **8**, 11297 (2018).
57. Peramaiyan, G., Sankar, R., Muthuselvam, I. P. & Lee, W.-L. Anisotropic magnetotransport and extremely large magnetoresistance in NbAs_2 single crystals. *Sci. Rep.* **8**, 6414 (2018).

ACKNOWLEDGEMENTS

We sincerely thank Simin Nie, Zhipun Wang, and Mohammad Saghayezhian for fruitful discussion. This work was primarily supported by the U.S. Department of Energy under EPSCoR Grant No. DE-SC0012432 with additional support from the Louisiana Board of Regents. R.N., E.W.P., and R.J. also acknowledge the support by the National Science Foundation through DMR-1504226.

AUTHOR CONTRIBUTIONS

R.J. designed research; A.S. synthesized the sample and conducted physical property measurements with assistance from R.C., L.X., D.G., R.N., D.P.Y., and E.W.P.; X.G. and W.X. conducted single crystal XRD measurements; A.S. and R.J. wrote the manuscript with contributions from all the authors.

COMPETING INTERESTS

The authors declare no competing interests.

ADDITIONAL INFORMATION

Correspondence and requests for materials should be addressed to R.J.

Reprints and permission information is available at <http://www.nature.com/reprints>

Publisher's note Springer Nature remains neutral with regard to jurisdictional claims in published maps and institutional affiliations.



Open Access This article is licensed under a Creative Commons Attribution 4.0 International License, which permits use, sharing, adaptation, distribution and reproduction in any medium or format, as long as you give appropriate credit to the original author(s) and the source, provide a link to the Creative Commons license, and indicate if changes were made. The images or other third party material in this article are included in the article's Creative Commons license, unless indicated otherwise in a credit line to the material. If material is not included in the article's Creative Commons license and your intended use is not permitted by statutory regulation or exceeds the permitted use, you will need to obtain permission directly from the copyright holder. To view a copy of this license, visit <http://creativecommons.org/licenses/by/4.0/>.

© The Author(s) 2020